Laparoscopic Renal Denervation System for Treating Resistant Hypertension: Overcoming Limitations of Catheter-based Approaches

Jinhwan Baik[†], Won Hoon Song[†], Donghyun Yim, Sangyong Lee, Sunchoel Yang, Hae-Yong Lee, Eue-Keun Choi, and Chang Wook Jeong[*] & Sung-Min Park[*]

Abstract— Goal: **In a pivotal clinical trial, the percutaneous catheter-based renal denervation system developed to treat resistant hypertension did not show effectiveness in reducing blood pressure because of its fundamental limitation to ablate deeper nerves present around the renal artery.** *Methods:* **We propose a new renal denervation strategy called laparoscopic denervation system (LDS) based-on laparoscopy procedure to ablate the renal nerves completely but inhibit the thermal arterial damage. The system has flexible electrodes to bend around the arterial wall to ablate nerves The simulation study using validated in-silico models evaluated the heat distribution on the outer arterial wall, and an acute animal study (swine model) was conducted to demonstrate the feasibility of LDS** *in vivo.* *Results:* **The simulation study confirmed that LDS could localize the heat distribution between the electrode and the outer arterial wall. In the animal study, we could maximize nerve denervation by the localizing ablation energy within the renal nerves and achieve nerve denaturation and decrease in neural density by 20.78 % (P<0.001), while maintaining a constant tip temperature of 65 ℃ for the duration of 70 s treatment. The study confirmed intact lumen artery through histological analysis and acute reduction in systolic blood pressure by 9.55 mmHg (p<0.001)** *Conclusion:* **The LDS presented here has potential to effectively and safely ablate the renal nerves, independent of anatomical variation and nerve distribution, to control hypertension in real clinical conditions.** *Significance:* **LDS approach is innovative, inventive, and presents a novel technique to treat hypertension.**

Index Terms—**Hypertension, denervation, animals, laparoscopy, radiofrequency ablation, finite element modeling**

I. INTRODUCTION

Hypertension is the most common disease in humankind with a current global prevalence of about 1.39 billion, which accounts for 31.1% of the adult population and is expected to keep increasing [1, 2]. Despite hypertension being the leading global disease burden, ironically, it is also the leading preventable risk factor of death and disability worldwide [3]. Many antihypertensive drugs have been developed over decades and available in the market. However, a large proportion of patients' blood pressure still remains uncontrolled because of resistant hypertension [4]. Resistant hypertension is defined as a disease in which blood pressure (BP) cannot be controlled despite the concurrent use of 3 or more antihypertensive drug combinations [5]. One pooled analysis estimated that the prevalence of this life-threatening resistant hypertension is 10.1% of adults being treated for hypertension [6].

The hyperactivity of the renal sympathetic nerve is known to be an important pathogenesis of essential and resistant hypertension [7]. In the early 60s, sympathectomy, which surgically destroys the thoracic and lumbar sympathetic ganglia, was introduced to control the sympathetic nerve and thus to treat resistant hypertension [8]. This method clearly showed a postoperative decrease in BP and survival benefits [8, 9]. However, due to the severe invasiveness and morbidity associated with the surgical procedure, this method was abandoned from the practice [10]. Then, percutaneous catheter-based renal denervation (RDN) has been recently proposed as an alternative for treating resistant hypertension with reduced invasiveness [11, 12]. This concept initially gained large traction due to its minimal invasiveness and promising initial data [11, 13]. However, a recently conducted phase III randomized controlled trial showed that this approach showed no effectiveness in BP reduction when compared to sham control [14]. The failure of catheter-based RDN can be attributed due to many reasons as outlined in [15].

While it cannot be generalized, the lesion depth for the catheter-based RDN was found to be about 2 mm for a cadaver

W. Song is with the Department of Urology, Pusan National University Yangsan Hospital, Yangsan, Republic of Korea.

S. Lee and S. Yang are with the Department of Prototype Production, Osong Medical Innovation Foundation, Chungbuk, Republic of Korea.

H. Lee and E. Choi are with the Department of Internal Medicine, Seoul National University Hospital, Seoul, Republic of Korea.

C. Jeong is with the Department of Urology, Seoul National University Hospital, Seoul, Republic of Korea (e-mail: drboss@snu.ac.kr)
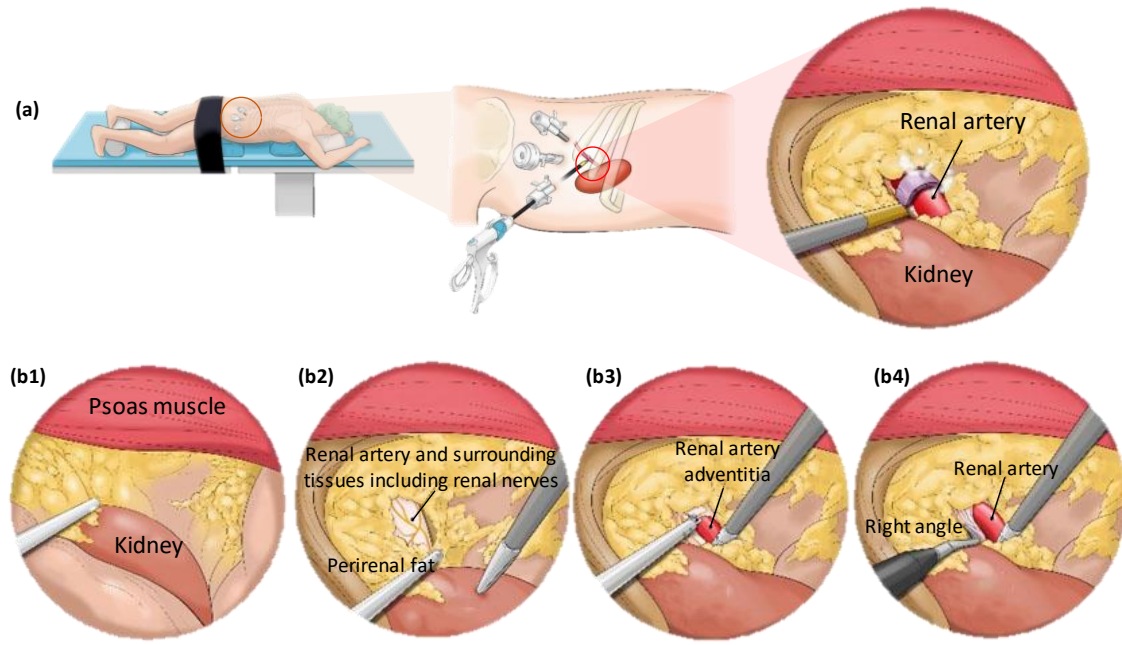
Fig. 1. Laparoscopic renal denervation. (a) The modified prone position for the laparoscopic RDN. (b) Schematic to show the steps of laparoscopic RDN; b1, Dissection between Psoas muscle and Gerota's fascia; b2, Removal of fat tissues around the renal hilum and identification of connective tissues surrounding the renal artery including renal sympathetic nerves; b3, Removal of peri-arterial connective tissue using a laparoscopic monopolar hook electrode; b4, Securing space to insert the laparoscopic ablation instrument using right angle dissector.

[16] and 6 mm for animal models [17-19] from multiple studies, but 31% of renal nerves are located 2-10 mm away from the endoluminal surface [20, 21]. Thus, it cannot completely ablate renal sympathetic nerves outside the arterial wall. Increasing the ablation energy to reach beyond 2 mm would cause irreversible intima injury resulting in serious complications such as atherosclerosis, thrombosis, or stenosis [22, 23]. Furthermore, the catheter denervation is only applicable to the renal artery with a diameter $\geq$ 3mm. However, small arteries, such as accessory arteries or early branched arteries, also have nerves that still have a significant effect on controlling BP [24, 25]. Also, the catheter-based modality requires expertise to guide the catheter from aorta to the main renal artery [15].

Thus a procedure to effectively ablate renal nerves while not being as invasive as sympathectomy is needed to treat the resistant hypertension patients. The system should also be safe, operator-independent, and achieve complete denervation. As explained in our previous simulation study, our hypothesis was that the solution to satisfy these unmet needs could be found in a laparoscopic approach [17]. The laparoscopic RDN provides more effective denervation compared to the catheter-based RDN and is independent of anatomical variation in the renal artery and nerve distribution. It also achieves the denervation without injuring the artery [17] and its adjacent organs. Even though the proposed laparoscopy-based technique is more invasive compared to catheter-based RDN, it enhances the safety against thermal damage to the artery and the nerve denervation is more effective than the catheter-based approach.

In this paper, we present a novel laparoscopic denervation system (LDS) and provide surgical guidelines for applying laparoscopic RDN in clinical trials. The system is composed of a laparoscopic instrument with a round-shaped flexible electrode and an automatic ablation temperature control system.
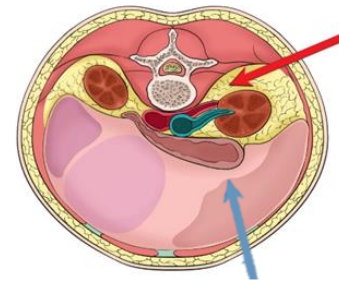

Fig. 2. Retroperitoneal approach (red) and transperitoneal approach (blue)

In the next few sections, we will present details of the LDS system along with the simulation and validation experiment. Next, we will utilize *in-vivo* simulation and cumulative equivalent minutes at 43℃ (CEM43) to guide first-time *in-vivo* study using LDS. Finally, we will demonstrate the feasibility of LDS in animal studies using a swine model and conclude with a discussion.

II. LAPAROSCOPIC DENERVATION SYSTEM

Fig. 1a shows our proposed laparoscopic RDN system, and the procedure is illustrated in Fig. 1b. If the procedure is conducted through the posterior retroperitoneal approach, as shown in Fig. 2, it provides direct access to the renal arteries without affecting intraperitoneal organs. This approach presents a significant advantage compared to the transperitoneal approach, where the laparoscopic trocar punctures the peritoneum and passes through the intraperitoneal organs before accessing the retroperitoneal space. After a patient is positioned in the modified prone position like Fig. 1a, the procedure followed is as follows: (1) dissect between psoas muscle and kidney to access renal hilum; (2) remove fat tissues around the renal hilum of kidney, and identify connective tissues and renal sympathetic nerves surrounding the renal
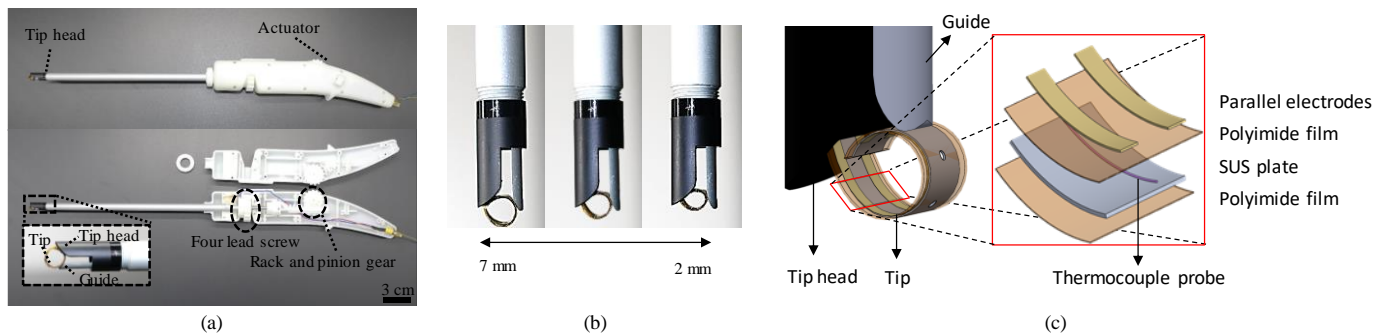
Fig. 3. Designs and materials for the ablation instrument. (a) A minimally invasive laparoscopic ablation instrument. (b) Flexible tip diameter is changed from 7 mm to 2 mm to cover various sizes of arteries. (c) Laminated tip stacked with laminations in the following order from the bottom: polyimide film, SUS plate, thermocouple probe, polyimide, and bipolar electrode.

artery; (3) remove the peri-arterial connective tissue meticulously using a laparoscopic instrument such as monopolar hook electrode; (4) secure the space to insert the laparoscopic ablation instrument; and (5) insert the instrument through a 5mm working port to ablate renal sympathetic nerves around the renal artery by wrapping it 360 degrees. During the 4th step, make sure all surrounding tissue between the renal artery and renal vein is secured. If the patient has an additional artery or early branch, repeat the procedure (2) through (5).

The retroperitoneal surgical space is limited, and target nerves are randomly distributed around various size arteries. Thus, the three main requirements of laparoscopic instrument design for RDN are: (1) should be able to automatically wrap both renal artery and nerves for effective denervation regardless of the nerve distribution, (2) should prevent thermal damage to tunica intima by concentrating heat between the instrument tip and the outer wall of the artery, and (3) should be available in various sizes to cover main artery, accessory artery, and early-branching artery.

A. Bipolar flexible electrode

The prototype of our ablation instrument meeting all three requirements is shown in Fig. 3a. It is composed of two parts; electrical ablation tip and mechanical actuator. The electrical ablation tip, as shown in Fig. 3c contains a biocompatible heat-treated stainless steel (SUS) plate that changes shape from straight to round when extruded from tip head, and it maintains its round shape without external load. The SUS plate is coated with a flexible printed circuit board (FPCB), where parallel copper-coated-gold electrodes are attached over polyimide film. The parallel electrodes form bipolar configuration localizing electrical current path between the electrodes, and the concentration results in heat generation at tissue. This configuration confines the heat between the electrode surface and the outer wall of the artery.

The actuator part includes a rack, pinion gear, and a four lead screw. The rack and pinion gear facilitate the surgical operation to bind the renal artery, as shown in Fig. 3a, by simple back and forth manipulation of the gear without needing manual handling. The four lead screws adjust the tip diameter from 7 mm to 2 mm, as shown in Fig 3b, and controls the guide to tighten the ablation tip for tight contact with various sizes of renal arteries. Furthermore, we performed repeatability testing of tip bending
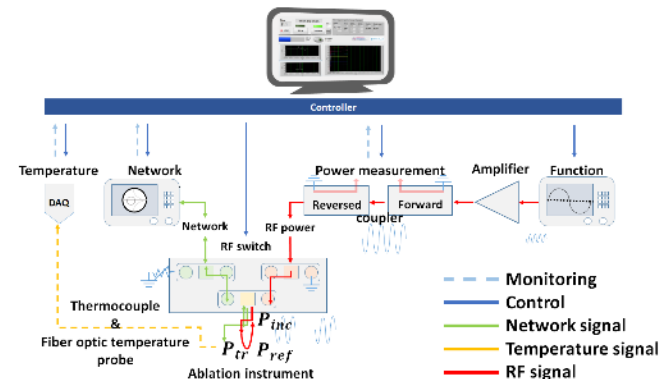

Fig. 4. The configuration of automatic ablation temperature control system. The system measures tip temperature, load impedance, incident power P_{inc}, reflected power P_{ref}, and transmitted power P_{tr}.

and the unrolling process. Even after twenty or more repeated processes during lab testing and preclinical study, the ablation tip preserved round shape to successfully cover the renal artery and nerves.

B. Automatic ablation temperature control system

To minimize forming thermal lesion during denervation and to prevent damaging tunica intima, we use temperature-controlled radiofrequency (RF) ablation [26]. In temperature-controlled ablation, the temperature is maintained constant through the procedure. We use an automatic ablation temperature control system, as shown in Fig. 4, to control the temperature. It consists of a function generator (AFG3101, Tektronix), an RF power amplifier (LZY-22+, Mini-circuits), two bi-directional couplers (ZABDC50-150HP+, Mini-circuits), two power sensors (U2004A, Keysight Technologies), a vector network analyzer (E5061B, Keysight Technologies), a three single pole double throw type of RF switch (USB-4SPDT-A18, Mini-circuits), an analog-to-digital converter (DAQ, NI9213, National Instruments), and a computer controller (LabVIEW, National Instruments). The controller simultaneously controls the function generator, RF switch, VNA, power sensors, and DAQ and also monitors: (1) tip temperature, (2) transmitted and reflected RF power at power sensors connected to directional couplers, and (3) impedance between parallel electrodes at VNA with frequency varying from 1 kHz to 10MHz.

Before the treatment begins, the system sets the input RF power level taking into consideration the reflected power caused by the impedance mismatch between the system output

and the ablation instrument. During treatment, the function generator delivered 1 MHz RF signal and amplified RF power to heat the ablation tip. The power is modulated by changing the RF switching time with the pulse-width-modulation (PWM) method to maintain a constant tip temperature. The RF switch connects the ablation instrument to the amplified RF power in the "On state" of the PWM and the VNA in the "Off state" of the PWM. A feedback control system decides the period and duty cycle of the PWM by comparing the monitored tip temperature with pre-set tip temperature.

III. FINITE ELEMENT METHOD MODELING

To achieve complete RDN while preventing damage to arterial wall and vein, we analyzed temperature distribution during denervation with thermoelectrical finite element modeling (FEM) using ANSYS Fluent. The peak temperature and duration of ablation determined by the simulation study are used to control RF ablation during the animal study.

The Bio-heat equation is the governing equation to obtain thermal distribution in tissue. The equation below describes the coupled electric and thermal problems [27, 28].

$$\rho c \frac{\partial T}{\partial t} = \nabla \cdot k \nabla T + q - Q_{cooling} + Q_{meta} \quad (1)$$

where T is temperature, t is time, and other parameters are thermal properties: thermal conductivity of tissue k, the specific heat of tissue c, and mass density of tissue ρ; electrical properties: heat source from electrical energy q; and temperature cooling effect caused by blood or airflow $Q_{cooling}$. In this simulation study, we ignored the metabolic heat Q_{meta} since it is negligible compared to others [27].

With respect to the electric problem, the 1 MHz wavelength of the signal used in LDS is more than the size of the flexible electrode wrapping the renal artery and nerves. Therefore a quasi-static approximation was applied to solve the electric fields in the renal artery and nerves [29]. A governing equation used to solve electrical potential in tissue is given by:

$$\nabla \cdot \sigma \nabla V = 0 \quad (2)$$

where σ is the electrical conductivity of tissue, and V is electrical potential. The electric field is the gradient of electrical potential.

$$E = -\nabla V \quad (3)$$

The heat source term q was calculated using Ohm's law.

$$q = J \cdot E = \sigma(\nabla V)^2 \quad (4)$$

The electrical conductivity of tissue is temperature-dependent and is as given by:

$$\sigma(T) = \sigma_0(1 + k\Delta T) \quad (5)$$

where σ is electrical conductivity, σ_0 is reference electrical conductivity at 25°C, k is the temperature constant, and ΔT is the temperature difference from 25°C. We set the temperature constant at 2%°C^{-1}. A convection effect was applied at the outer arterial wall as a boundary condition:

$$Q_{air} = h(T - T_0) \quad (6)$$

We assumed free convection at walls exposed to CO_2 gas with convective heat transfer coefficient (h) of 25 Wm-2K-1 and free stream temperature (T_0) of 300 K. In laparoscopic renal denervation, due to the detachment of target renal artery from
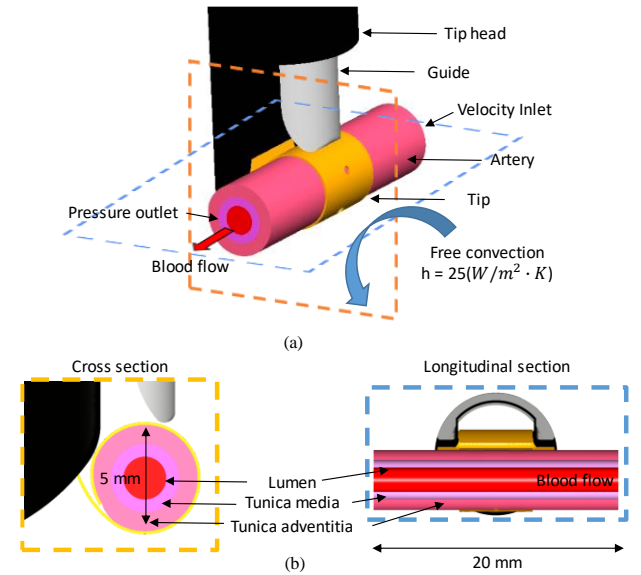

Fig. 5. (a) Configuration of modeled laparoscopic renal denervation and (b) detailed geometry of the cross section and longitudinal section across instrument tip.

fat, periarterial connective tissue and capillaries, the blood perfusion in the artery will be decreased. In addition, the cooling effect by bulk blood flow in this detached artery is more dominant than blood perfusion [30]. Therefore, we used fluid flow to simulate blood cooling effect and not blood perfusion in the lumen of the artery. Blood cooling effect (Q_{blood}) was simulated using a velocity inlet (blood flow rate) and a static pressure outlet as 0 Pa. In ANSYS Fluent, the Bio-heat equation was coded and applied to model via a built-in user-defined function. Using the user-defined scalar and the specified value at both electrodes, with zero specified flux at the other parts, we simulated the transient situation with 1 second time step size and 90-time steps in *in vitro* stimulation and the steady-state situation *in vivo* simulation. In the animal study, the ablation tip temperature remained constant due to the automatic ablation temperature control system.

In vitro simulation, the phantom gel surrounds the ablation tip, guide, and tip head. The material's density, specific heat, electrical conductivity, and thermal conductivity of each material are illustrated in Table I [28, 31-35]. In phantom, we measured electrical conductivity by an impedance analyzer

TABLE I
PROPERTIES USED IN THE MODEL AND THE VALIDATION EXPERIMENT

Material	mass density (kg/m^3)	specific heat $(J/kg \cdot K)$	thermal conductivity $(W/m \cdot K)$	electrical conductivity (S/m)
Phantom gel [a]	1000	4187	*Sensitivity analysis	0.648
**Blood [b, c]	1060	3890	0.531	0.67
Tunica adventitia [b]	1027	2372	0.39	0.392
Tunica media [b, d]	1050	3314	0.450	0.33
SUS304 [e]	8000	500	16.2	1.39 x 10^6
Polyimide	1420	1090	0.12	6.6 x 10^{-16}

*Sensitivity analysis: 0.48, 0.49, 0.50
**Blood flow rate: 0.28, 0.48, 0.68 (m/s)
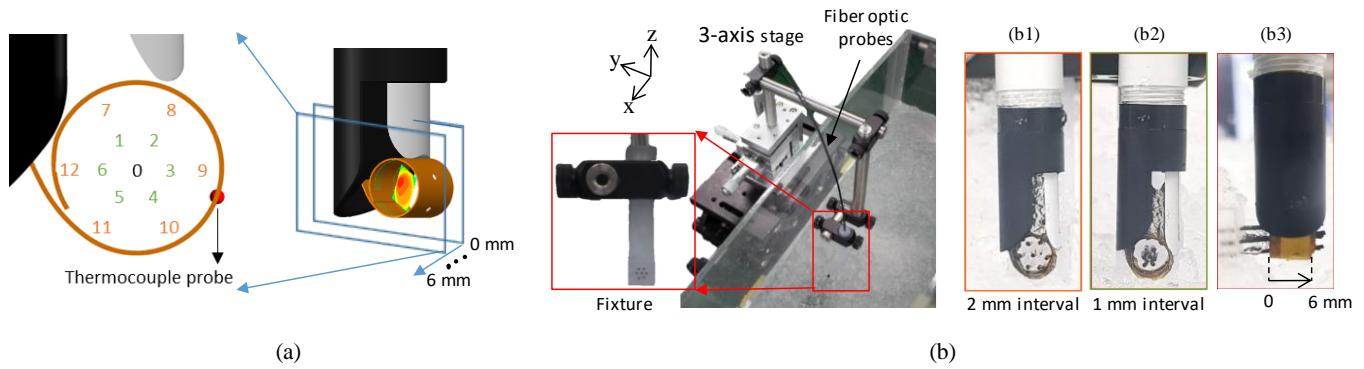[a]Park, [b]Duck, [c]Golombeck, [d]Edgerton, [e]Chen

Fig. 6. The experiment of parameter-controlling phantom gel. (a) Geometry of the FEM model (13 temperature measurement points and a thermocouple probe) (b) Experimental setup of RF heating using the flexible electrode; b1, Temperature measurement points are 0 and 7–12; b2, Temperature measurement points are 0–6; b3, Monitoring points 0 and 7–12 at x=6 mm plane. (Temperature are monitored at the tip of the probes)

(E4990A, Keysight Technologies) with a liquid test fixture (16452A, Keysight Technologies), calculated material's density, and considered the specific heat of the gel as the value of water. We also performed sensitivity analyses to test the effect of temperature dependency as the thermal conductivity of the phantom was varied from 0.48 to 0.5 in the temperature range 37-97 ℃ [36].

After establishing the validity of using the meshing method, bio-heat equation, and setting boundary conditions *in vitro*, we extended these techniques to *in-vivo* simulation with the renal artery model. In *in-vivo* simulation, the artery 3D, as shown in Fig. 5 was designed based on previous histological studies where the diameter of the artery, the diameter of the lumen, and thickness of the artery wall were 5 mm, 2mm, and 1.5 mm, respectively [17, 21]. The arterial wall was composed of tunica media and adventitia. To analyze heat distribution in various *in-vivo* studies, we changed the ratio of the thickness of the tunica media and adventitia while maintaining the total diameter of the artery as 5 mm. Compared to the phantom gel in *in-vitro* modeling, in *in vivo* arterial blood flow was taken into account with the flow rates from 0.28 to 0.68 m/s [37]. The blood temperature was set as 310 K with other conditions remaining the same. At electrode-tissue interfaces, the electric potential of an electrode in Fig. 3c was zero. The electric potential of the other electrode was chosen to make the temperature between the two electrodes at 60 or 65 ℃ in the steady-state condition. The modeling domain was a cuboid with 30 mm (height) x 20 mm (length) x 20 mm (width) in the phantom simulation. The artery was of the cylinder in shape with a height of 20 mm and a radius of 2.5 mm *in vivo* simulation. The default element size was 0.1 mm, and the element size near the electrodes was 0.05 mm.

IV. VALIDATION OF THE MODEL

Fig. 6b shows the validation experiment setup and applied 1 W RF energy to the instrument for 90 seconds. The phantom was manufactured by mixing 6 L water with 48 g gelling agent (polyacrylic acid solution, Sigma-Aldrich) in a 160 mm×430mm×170mm acrylic water tank. In this phantom gel, we considered that the convection effect was almost zero, mass density and specific heat were the same with water. The electrical conductivity of the phantom was measured using an

impedance analyzer (E4990A, Keysight Technologies).

We used fiber optic temperature probes (STB Probe, Luxtron Corporation) combined with data acquisitions (system M604, Luxtron Corporation) to measure the temperature distribution. The probes measured temperature at the tip of the probe using light and set up minimizes the electromagnetic interference. The temperature probes were fixed to two types of 3D printed fixtures (Project MJP 2500, 3D Systems). Fig. 6b shows two types of fixtures. The sides of a hexagon in one fixture was 1 mm and the second fixture was 2 mm. The fixtures have 7 temperature probe holders with one each at 6 vertices and one at the center of the hexagon. A fixture was anchored to a 3-axis stage, tuned for the 7 probes located at a side of electrode (x=0 or 6 mm plane), and coordinated with the center of the flexible electrode. Next, the fixture moved 0.5 mm from one side of the electrode to the other side, whose width was 6 mm. The measurements were repeated with the other fixture. There were 13 temperature measurement points in a plane, as shown in Fig. 6a and total points were 169 ((6+6+1)×13), where we assumed the center of two fixtures being the same.

The temperature at the location of the thermocouple probe and 169 points corresponding to the position of fiber optic temperature probes were post-processed. For facilitating comparison between modeling and experimental data, the temperature at point i (1≤i≤169, where i is an integer) was normalized using the formula:

$$NT_{\exp_i} = \frac{T_{\exp_i} - 300}{T_{\exp_c} - 300} \tag{7}$$

$$NT_{FEM_i} = \frac{T_{FEM_i} - 300}{T_{FEM_c} - 300} \tag{8}$$

where $NT_{\exp_i}$ is the experimental normalized temperature at point i, $T_{\exp_i}$ is the experimental temperature (K) measured at point i, and $T_{\exp_c}$ is the experimental temperature (K) at thermocouple. $T_{\exp_i}$ was standardized with $T_{\exp_c}$ because inserted thermocouple between FPCB and SUS plate and its position remained unchanged. The 300 (K) was subtracted from $T_{\exp_i}$ and $T_{\exp_c}$ considering the initial room temperature. NT_{FEM_i} is described using Eq. (8) in the similar manner. Relative error between $NT_{\exp_i}$ and NT_{FEM_i} was calculated by:

$$\text{Relative Error (\%)} = \left| \frac{NT_{exp_i} - NT_{FEM_i}}{NT_{exp_i}} \right| \times 100 \qquad (9)$$

V. ANIMAL STUDY

A. Surgical protocol

Since the LDS is for a new concept of surgery, there were no specific guidelines for surgical protocols of laparoscopic RDN, such as ablation temperature or duration of treatment. To guide the ablation temperature *in-vivo* experiment, we used heat distribution results from *in-vivo* simulation. In addition, the duration of treatment was determined by cumulative equivalent minutes at 43℃ (CEM 43), which is a thermal dose unit used for determining damage threshold for a specific tissue [38, 39]. The CEM 43 is calculated using the equation (10):

$$\text{CEM 43} = \sum_{t=o}^{t=final} R^{(43-T)} \Delta T, \ R = \begin{cases} 0.25, & T < 43\,℃ \\ 0.5, & T \geq 43\,℃ \end{cases} \quad (10)$$

where t is time (min), T is the temperature (℃) at time t, and R is a constant value.

In this study, mid-line incision was performed with the swine in the supine position, and open surgery was performed to confirm the feasibility of the LDS. The Fig. 7 shows the timeline of the protocol in an animal study. After anesthesia, we inserted the catheter for BP monitoring and incised the bladder to drain the urine during the study. We ablated renal nerves bilaterally using LDS on a main, accessory, and branched arteries. The ablation duration was set to 70 seconds, which was based on the *in vivo* simulation results. The total maximum RDN procedure time was 20 min. After completing the surgery, renal arteries with nerves were harvested for immunohistochemical evaluation, and swine were euthanized. As a metric of effectiveness, we measured the acute change in BP after RDN.

B. Swine model

The performance of LDS and the ablation protocol were evaluated using a swine model. The swine is physiologically and anatomically similar to humans and are most commonly used in preclinical studies of cardiovascular devices [40].

Seven swine of 45 kg each were NPO for 12 h and then were injected preoperatively with 0.06 mL/kg of Tardomyocel comp. III antibiotic. Sedation was induced by intramuscular application of zoletil (5 mg/kg) and xylazine (2 mg/kg). The preoxygenation using the facial mask and tracheal intubation was performed, and the depth of anesthesia was maintained under 2.0 to 2.5% of isoflurane with normoxia (SpO2 98%) and normocapnia (EtCO2 38-40 mmHg). Intravenous infusion of

Fig. 7. Timeline of LDS procedure protocol in an animal study

normal saline maintained central venous pressure between 6 and 8 mmHg.

C. Blood pressure acquisition and analysis

A sheath and catheter were inserted into the carotid artery, and the catheter nozzle was connected to a transducer for continuous monitoring of BP. The transducer was connected to a data acquisition system (iWorx RA-834 Recorder, iWorx Systems Inc) for further data processing, whose sampling rate is 100 sample/s. Anticoagulation was maintained with continuous intravenous bolus injection (40–50 IU/kg/h) of the unfractionated heparin. During the experiment, the depth of anesthesia was kept constant, and body surface ECG and pulse oximetry were monitored.

To test the acute BP change due to RDN, we compared paired BP samples in a swine model, as shown in Fig. 7. After incising the bladder and finding the renal artery, we waited for BP to be stabilized before obtaining the baseline BP. The BP was expressed as the mean of arterial BP (MAP) and systolic BP (SBP) and was calculated at the last 2 minutes of steady-state. The BP after RDN was also acquired in a similar manner. We carried out a sham surgical control study except performing RDN. In the sham control study, the LDS procedure was stopped right after incising the bladder and the peritoneum near renal hilum. Care was taken not to damage any renal nerves located in the periarterial connective tissue. After BP was stable, we compared the initial BP (baseline) with the BP after 20 minutes since the RND procedure took about 20 minutes.

D. Immunohistochemical evaluation

Each renal artery was fixed in 4% formalin for 24 hours, paraffin-embedded, and was then sectioned at 200 um intervals. For each section, 10 serial slides were cut with 4 um thickness. The quantitative analysis of protein denaturation and necrosis of renal sympathetic nerves around renal arteries was performed using hematoxylin and eosin (H&E) staining. The endothelial damage and smooth muscle fibrosis of renal arteries were assessed using Masson's trichrome (MT) staining.

E. Quantitative histological analysis

Stained tissue slides were examined under digital pathology scanner (Aperio AT2, Leica) and were magnified 30, 200, and 400 times by the pathology slide viewing software (Aperio ImageScope, Leica). We classified tissue slides into the control group and treatment group using 30 times magnification pictures. We labeled 71 nerves between those two groups and quantized the intensity and percent area fraction of the pixels that are the positive reaction for staining agents on 200 times magnification pictures. This was conducted on the image processing software (ImageJ software, National Institute of Health) [41-43]. The software calculated the mean intensity of the positive reaction area by averaging all RGB intensity within the region of interest of H&E stained image. The picture was separated via color decomposition as red, blue, and green when the positive reaction area was estimated. The area of blue in the deconvolution picture was calculated by adding all pixels over a specific threshold, which was decided by a previously reported iterative procedure based algorithm [44]. Finally, we calculated the change in the intensity and percent area fraction between non-ablation group and ablation group and found a
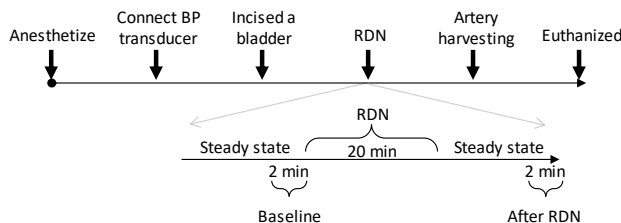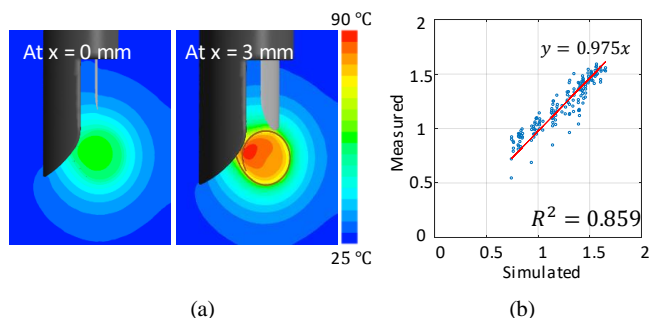
(a)   (b)

Fig. 8. (a) Thermal distribution in the cross section of ablation tip in the FEM model of the phantom; at the side of the electrode (x=0 mm) and at the center of the electrode (x=3 mm). (b) Scatter plot of the temperature normalized by thermocouple probe showing the difference between the simulation and experimental results. (n=169, R^2=0.859)

correlation between the change of staining and area of renal nerves. To quantify the characteristic of nerves, we used distance from the lumen (mm) and nerve size (um). The distance was the length from the center of each nerve to the nearest endoluminal surface. The nerves size was the radius calculated from the nerve area by assuming a perfect circle.

F. Statistical analysis

All statistical analyses were performed using the SPSS v25 statistics tool (SPSS v25, IBM). All BP differences met the assumptions of normality and homogeneity of variance and were assessed by group t-test. All correlation analysis was performed by regression analysis.

VI. RESULTS

A. Thermal distribution of the bipolar flexible electrode

Fig. 8a shows the heat distribution at x =0 and x = 3 planes in the FEM model of the parameter-controlling phantom gel after heating 90 seconds. The simulated peak temperature distribution in x = 3 plane is higher than the temperature in x = 0 plane. The results confirm that the instrument could focus heat inside the instrument tip and between parallel electrodes. This simulation model was validated by comparing the simulated temperature profiles with experimental results at a total of 169 points (13 points for each 13 section planes). As shown in Fig. 6a, the temperature at the center of the tip is measured at 14 points, 13 points are for fiber optic temperature probe, and the final point is for the thermocouple probe integrated within the instrument. The simulation and experimental results of normalized temperatures measured by the thermocouple probes in simulation and experiment are shown in Fig. 8b using scatter plots. The coefficient of determination in the scatter is 0.859, and the overall average error is 6.97%. The effect of the thermal conductivity from the sensitivity analyses shows that the peak temperature did not differ more than 1.2℃ between simulations and experimental methods, which is an acceptable difference. This good agreement between the simulation study and validation experiments confirmed the credibility of the simulation method and modeling.

B. In vivo simulation and surgical protocol

We utilized a numerical simulation model to evaluate the thermal distribution at the ablation tip of the artery 3D model. The model's artery length, lumen diameter, the thickness of
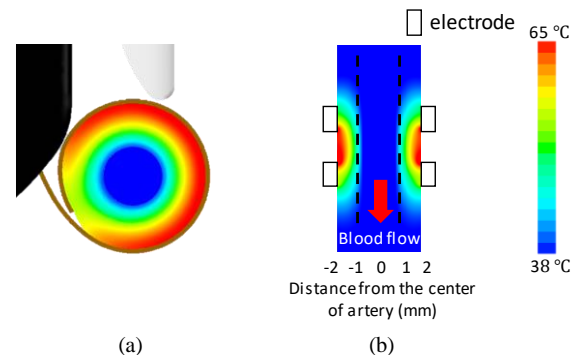

(a)   (b)

Fig. 9. (a) Thermal distribution at the cross section and (b) at the longitudinal section of 3D artery model with the tip temperature maintained 65 ° C.
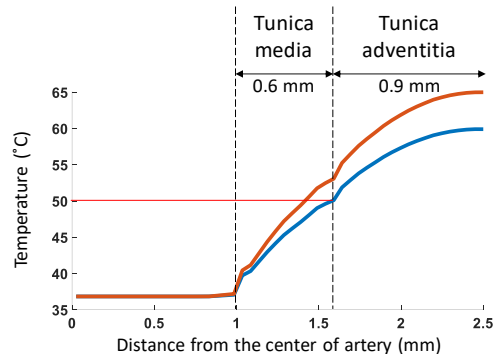

Fig. 10. Two-dimensional temperature profiles with constant tip temperature of 60 ° C (blue line) and 65 ° C (brown line). Red line is 50 ° C.
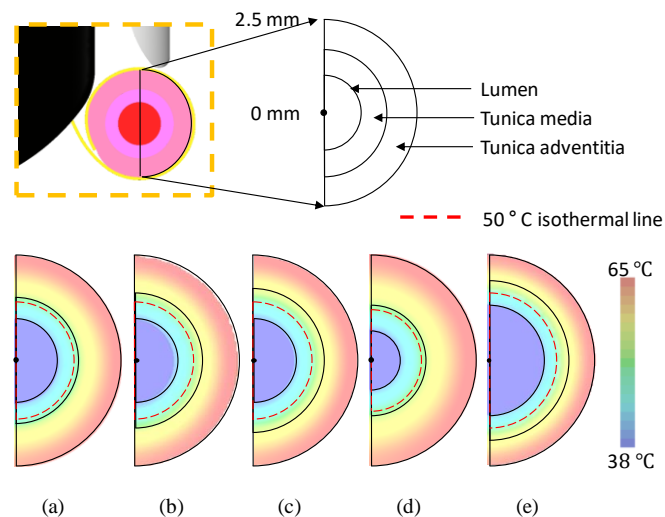

(a)   (b)   (c)   (d)   (e)

Fig. 11. Heat distribution in arteries with different sizes. (a) 2 x 0.5 x 1, (b) 2 x 0.6 x 0.9, (c) 2 x 0.7 x 0.8, (d) 1.4 x 0.6 x 1.2, and (e) 2.6 x 0.6 x 0.6; lumen diameter (mm) x thickness of tunica media (mm) x thickness of tunica adventitia (mm). (Blood flow rate = 0.68 m/s)

tunica media, and adventitia were set to 20 mm, 2 mm, 0.6 mm, and 0.9 mm respectively, with the blood flow rate set to 0.68 m/s, as shown in Fig. 5. With the tip temperature maintained at 65 ℃, the peak temperature distribution at the cross-section and the longitudinal section of the 3D artery model are shown in Fig. 9. The heat is concentrated on the outside of the artery, in the cross-section, and between the parallel electrodes in the longitudinal section. The temperature profiles at the center of two parallel electrodes are shown in Fig. 10.

We set 50 ℃ as an isothermal line, which is the thermal lesion boundary, or a nonviable volume [27]. Typically the renal

nerves distributed in tunica adventitia and periarterial connective tissue [20, 21]. Therefore, the ideal thermal lesion boundary should be located in the border between tunica media and adventitia while preventing thermal damage to tunica intima or lumen. Fig. 10 shows the border as a black dashed line at x = 1.6 mm. When the tip temperature remained at 60 ℃, the thermal lesion boundary was formed between tunica media and adventitia. As the tip temperature reached 65 ℃, the lesion boundary extended to the tunica media. In addition, we evaluated the thermal distribution with arteries of different sizes when ablating at a constant tip temperature of 65 ℃, as shown in Fig. 11. With the diameter of lumen fixed at 2 mm, the thermal lesion boundaries were at 1.4 mm from the center of the artery for various of tunica media thickness, e.g., 0.5 mm, 0.6 mm, and 0.7 mm. When the thickness of tunica media was fixed, and the diameter of the lumen was set at 1.4 mm and 2.6 mm, the thermal lesion boundaries were 1.2 mm and 1.6 mm, respectively, from the center of the artery. The electric potentials of an electrode in the simulation of Fig. 11(a-e) were 20, 20.2, 20.3, 17.3, and 24.3 V. When the blood flow rate in the artery was varied, 0.28, 0.48 and 0.68 m/s, the thermal lesion boundaries were about 1.39 mm from the center of the artery, and the electrode electric potentials were 19.7, 19.9, and 20.2 V, respectively. These results show that the ablation with a constant tip temperature generated the same heat distribution even when the blood flow rates were varied. Finally, from the simulation, we derived that the tip temperature should be 60 ℃ to 65 ℃ to completely ablate nerves while minimizing the damage on tunica intima.

The duration of treatment was determined by CEM 43. When expressing the damage threshold as CEM 43, the damage threshold for the artery of the pig (150 min) is higher than the damage threshold for nerves of the pig (80 min) [38, 45]. If temperature T is maintained at 50 ℃ during treatment, we could derive the treatment duration as 70 s after considering the threshold as CEM 43 of the renal artery, where the thermal dose at nerves must be more than the threshold needed to ablate the
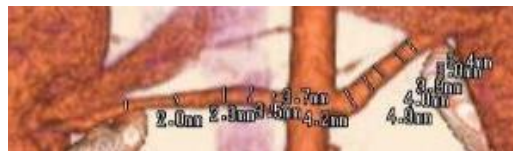

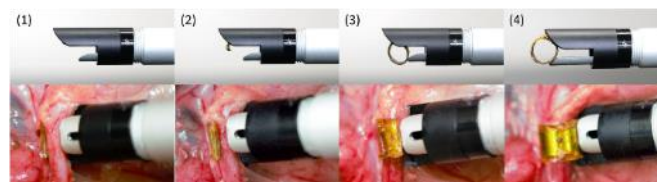Fig. 12. Computed tomography (CT) angiography of a porcine

Fig. 13. The process of electrosurgical instrument wrapping the renal artery

nerve. Using this process, we used the numerical simulation technique to guide the animal study protocol such that the tip temperature was between 60 ℃ and 65 ℃ with an ablation duration of 70 s for safe and effective renal denervation.

C. An animal study in a swine model

The Fig. 12 shows a computed tomography angiography of the first swine artery. In this figure, the diameter of the left and the right renal arteries are about 2 to 5 mm, which are easily covered by our designed instrument tip. Fig. 13 shows the process of our designed flexible electrode, wrapping the renal artery. For 12 arteries belonging to five swine model, we performed RDN 21 times (see Table II). The RF system took 7.14 s (±3.51) to reach 90% of pre-set tip temperature, called rising time, and percent maximum overshoot was 2.30 (±1.98) %.

The histological assessment at 4 sites of the ablated artery, i.e., farthest site (control), distal site, proximal site, and ablation site (treatment), are shown in Fig. 14a. Fig. 14b compares the H&E staining results at the farthest site with those at the ablation site. Fig. 14c shows the results of histological analysis at each location. Columns; (1-n) the farthest site away from the ablation, control group; (2-n) the distal site from the ablation; (3-n) the proximal site from the ablation; (4-n) the ablation site, treatment group. Rows; (n-1) overall morphological characteristics of nerves and artery (x30, H&E); (n-2) the closer

TABLE II
PERFORMANCE OF LDS IN ANIMAL STUDY

| Ablation #	Animal #	Target artery	Artery type	Position	Temp. (℃)	Rising time (s)	Maximum overshoot (%)
1	1	Left	Main	Proximal	60	2.59	2.28
2	1	Left	Main	Distal	60	4.39	-0.69
3	1	Right	Main	Proximal	65	4.33	-0.08
4	1	Right	Main	Distal	65	12.61	1.78
5	2	Left	Main	Proximal	65	14.99	1.60
6	2	Left	Main	Distal	65	6.80	2.54
7	2	Right	Main	Proximal	60	2.79	8.53
8	2	Right	Main	Distal	65	10.79	-0.11
9	2	Right	Accessory	-	65	7.00	4.79
10	3	Left	Branch	Distal	60	5.20	3.75
11	3	Left	Branch	Proximal	60	6.41	0.80
12	3	Left	Branch	-	60	8.59	2.98
13	3	Left	Main	-	60	3.79	0.52
14	3	Right	Main	Distal	60	6.19	2.63
15	3	Right	Main	Proximal	60	7.63	1.80
16	4	Left	Main	Distal	60	5.60	3.22
17	4	Left	Main	Proximal	60	7.80	2.67
18	4	Right	Main	-	60	6.81	0.65
19	5	Left	Main	-	60	6.61	2.83
20	5	Right	Main	Distal	60	15.20	4.18
21	5	Right	Main	Proximal	60	3.80	1.55
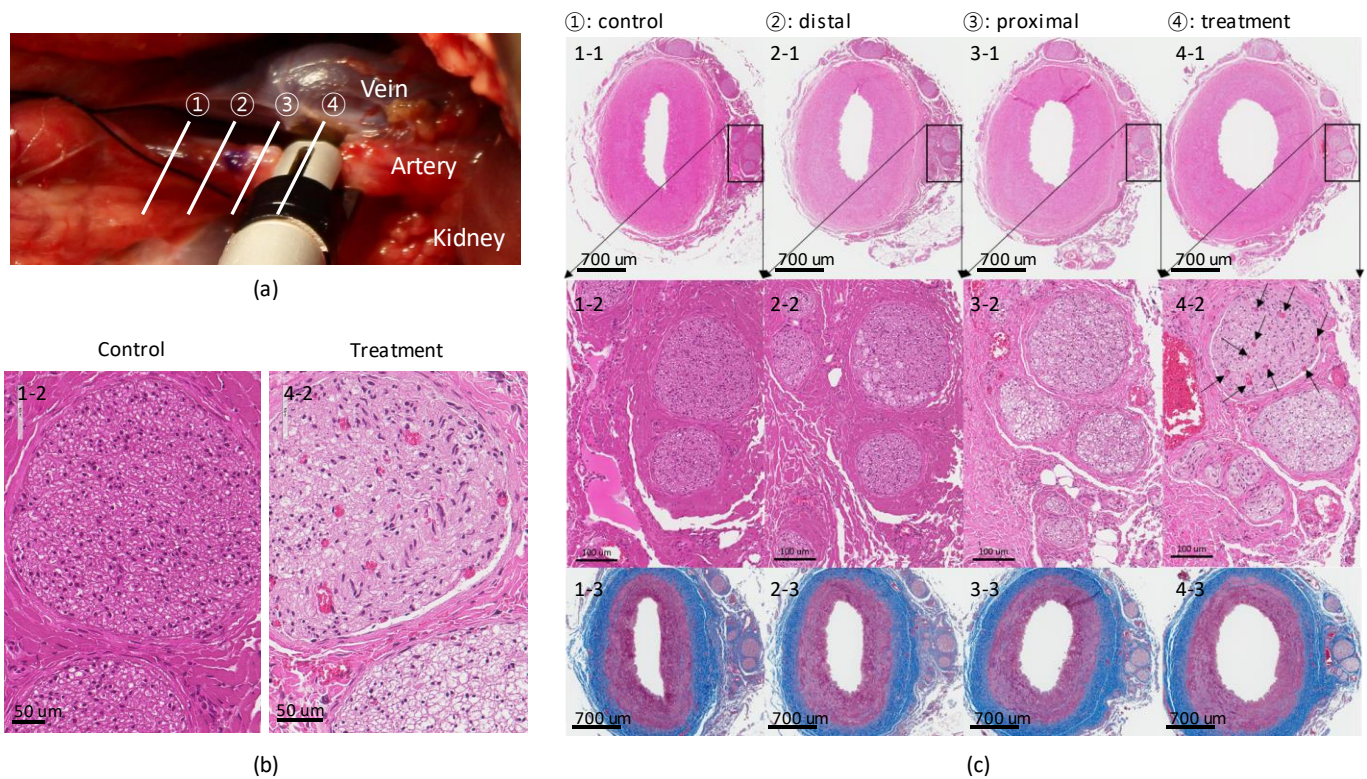
Fig. 14. Histological analysis of renal nerves and artery after RDN using LDS. (a) Histological assessment sections; 1. farthest site (control), 2. distal site, 3. proximal site, 4. ablation site (treatment). (b) Nerves stained with H&E at control and treatment section (x400). (c) Nerves and artery stained with H&E and MT at 1-4 sections. (H&E: hematoxylin and eosin, MT: masson's trichrome)

it is to the ablation site, the more noticeable denaturation of axons and neural fibers are, and the lower fiber density is (x200, H&E); (n-3) no arterial damage seen at any site (x30, MT). Arrows at 4-2 are hemorrhage. In the results of H&E staining, as shown in the first and second row of Fig. 14c, the closer the tissue is to the ablation site, the more noticeable denaturation of axons and neural fibers are and lower the fiber density is. The histology showed some hemorrhage at the ablation site inside nerves. On the other hand, no arterial damage is detected at any site, as shown in the third row of Fig. 14c, via MT staining. The arterial damage in the tunica intima is detected only in one of the 12 arteries at MT staining.

Finally, BP is compared before and after RDN, as shown in Table III. There was an acute reduction in systolic blood pressure by 9.55 mmHg (p<0.001) and mean atrial pressure by 8.23 mmHg (p<0.001). In the sham control study, BP increased over time (p<0.001). The results of quantitative histology analysis after the evaluation of 71 renal nerves are shown in Fig. 11. Among the 71 nerves, the radius of 16 nerves (22.5%) were less than 50 um, 26 nerves (36.6%) were 50-100 um, 26 nerves (36.6%) were 100-200 um, and 3 nerves (4.2%) were over 200 um. With respect to distance, all nerves were located within 2.5 mm from the lumen. Comparing the control group and treatment group, the average difference in intensity and percent area fraction of positive reaction for H&E staining are 15.75 (p<0.001) and 20.78 % (p<0.001), respectively. When compared between ablation temperature at 60 ℃ (n=48) and 65 ℃ (n=23), the difference in ablation is distinctly larger at 65 ℃ compared to 60 ℃, as shown in Fig. 11c, and d. The average difference between the two groups in intensity and in percent

area fraction of positive reaction is 6.85 (p=0.031) and 8.42 (p=0.025). In Fig. 11e-h, the coefficients of determination in the scatter are 0.06 (p=0.521), 0.07 (p=0.474), 0.031 (p=0.143) and 0.106 (p=0.006) respectively, which showed the limited relationship exists between the reaction of staining and the nerve size or distribution.

VII. DISCUSSION

In this study, we presented a novel laparoscopic renal denervation system with a flexible electrode, which employs a direct nerve ablation technique by wrapping the renal artery. Our developed ablation instrument directly reaches the renal artery through retroperitoneal space and wraps both artery and nerves for effective nerve ablation at a constant ablation temperature. The flexible electrode can be utilized at various sizes of the artery and wraps all nerves independent of arterial anatomy and nerve distribution. During ablation, the electrode, which is composed of parallel bipolar electrodes, focuses on electrical current and heat distribution at the outer arterial wall for safe delivery of power. Furthermore, while the catheter-based system cannot measure nerve temperature directly, our LDS can directly measure the temperature of the outer arterial wall with a temperature probe embedded inside the ablation tip, which helps further in achieving effective and safe renal denervation. We showed proof of the concept of LDS via computational modeling and animal study.

The thermal distribution of the system was evaluated through both *in vitro* simulation and validation experiments. The good agreement between simulated and measured temperature
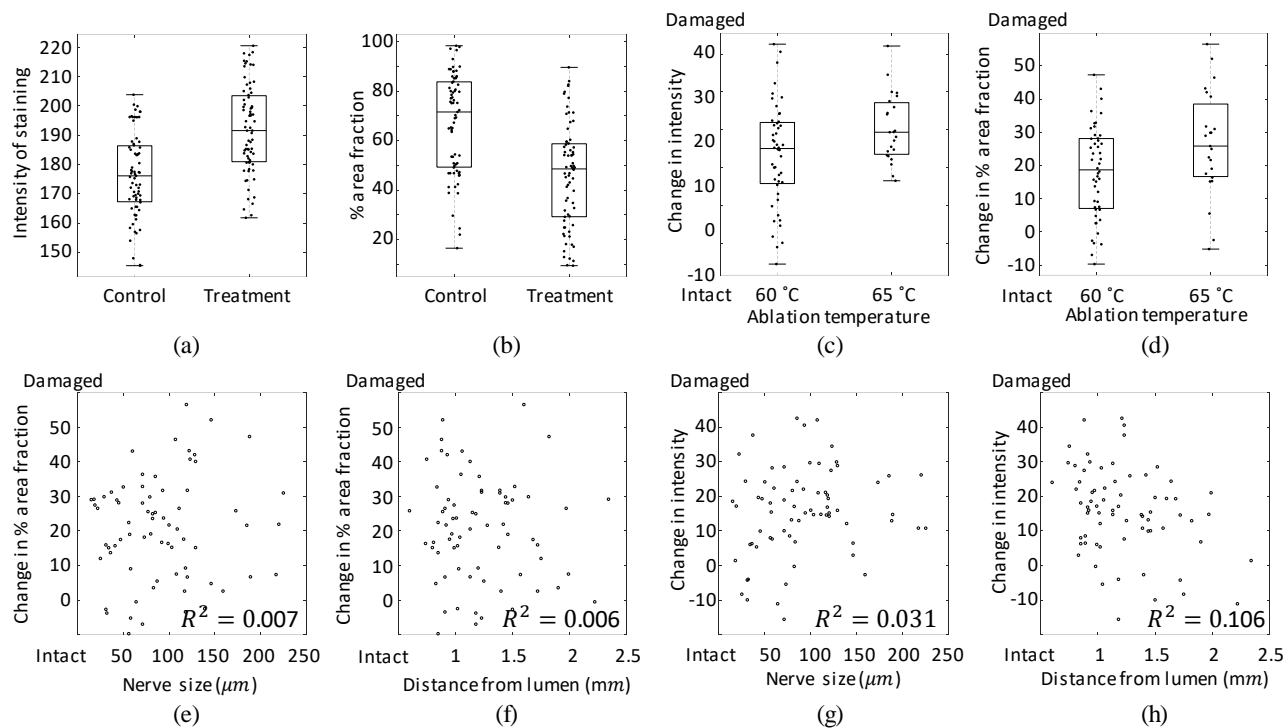
Fig. 15. Change in (a) Intensity and (b) percent area fraction for H&E stained nerves in control and treatment group. (c) Change in intensity of positive reaction and (d) in percent area fraction for ablation temperature of 60 ℃ (n=48) and 65 ℃ (n=23). (e-h) Scatter plot between the nerve size or distance from lumen and the change in percent area fraction or in intensity. Statistical significance (a) p<0.001, (b) p<0.001, (c) p=0.031, (d) p=0.025, (e) p=0.521, (f) p=0.474, (g) p=0.143, (h) p =0.006.

suggests that the uniform and focused heat distribution around the surface of the arterial wall, as suggested by the computational model, can be expected *in vivo*. *In vivo* simulation, we designed a 3D model where the flexible electrode only wrapped renal artery avoiding a renal vein and lymph nodes, since the peripheral tissues can change the electrical current path and thermal distribution [46]. After filling CO_2 gas into the abdomen and securing space to insert the laparoscopic instrument, as shown in Fig. 1b, the target renal artery begins to be detached from other tissues, as shown in Fig. 14a, and the flexible electrode will only wrap the artery. In this procedure, the tunica adventitia or connective tissue cannot be completely removed because of the risk of damaging the arteries. In addition, the exact ratio of the tunica media and adventitia thickness is difficult to determine. Thus, we analyzed the thermal distribution in arteries of different sizes using *in-vivo* simulation. The ratio of tunica media and adventitia did not affect the thermal lesion boundaries, but the total thickness of the arterial wall did affect the boundary. Thus, based on the *in vivo* simulation results and CEM 43, we set the surgical protocol for safe and effective delivery as follows: constant tip temperature of 60 ℃ or 65 ℃ and an ablation duration of 70 s.

Finally, we evaluated the preclinical applicability and safety of LDS. When the nerves in an animal study were compared between the treatment group and control group, the intensity and area fraction of positive reaction for histochemical were distinctly different. On the other hand, the arteries of these two groups were indistinguishable from each other and were confirmed via MT staining. The quantitative histology results showed that LDS will be able to damage all nerves regardless

of nerve's size and distance from the artery. The reanalysis results are along the lines of our expectation, showing more nerve damage at 65 ℃ when compared to 60 ℃, confirming the technique of the quantitative histology. Therefore, in an animal study using swine model, the flexible electrode could focus heat on the outer wall of the artery and effectively ablate renal nerves without arterial damage. Furthermore, since the depth of the thermal lesion does not increase in the constant-temperature ablation system, the duration of ablation can be adjusted to increase the thermal damage to the nerves [26]. Thus, while protecting the arterial walls of all types, LDS can completely damage all nerves by increasing the ablation duration.

In our normotensive animal model, to exclude the effects of

TABLE III
ACUTE BLOOD PRESSURE CHANGE AFTER RDN

Animal	Type	Baseline (mmHg)	After RDN (mmHg)	Diff. (After − Baseline)
Sham 1	SBP	103.94(±1.87)	107.96(±1.76)	4.02*
	MAP	93.54(±1.48)	97.35(±1.43)	3.81*
Sham 2	SBP	75.54(±2.51)	79.57(±2.40)	4.03*
	MAP	68.79(±2.24)	73.69(±2.13)	4.90*
1	SBP	72.32(±3.90)	67.09(±5.97)	-5.23*
	MAP	62.27(±2.89)	59.01(±4.86)	-3.25*
2	SBP	78.95(±3.54)	69.40(±4.73)	-9.55*
	MAP	69.95(±2.68)	60.71(±3.74)	-8.23*
3	SBP	116.57(±2.69)	116.40(±5.33)	-0.51 (p=0.742)
	MAP	96.79(±2.02)	96.88(±3.79)	-0.09 (p=0.806)
4	SBP	85.05(±4.31)	76.80(±4.71)	-8.25*
	MAP	72.31(±3.48)	65.06(±3.70)	-7.25*
5	SBP	83.04(±2.06)	79.14(±2.13)	-3.90*
	MAP	73.75(±1.69)	69.54(±1.73)	-4.23*

*P < 0.001

the drop in blood pressure by general anesthesia, sedation, drugs, or RDN procedures, the depth of anesthesia was approximately maintained throughout the operation. The renal denervation took approximately 20 minutes, and BP was measured after completing the renal denervation and achieving a stable state. We detected an acute decrease in BP after renal denervation, while the sham control study showed no meaningful change in BP. In the laparoscopic RDN procedure, the nerves at periarterial connective tissue (Fig. 1(b2)) were removed surgically, and those at tunica adventitia were damaged by LDS. Based on results from our study and previously published results [47, 48], we expect that the nerves located at and beyond 2.5 mm from lumen would be removed surgically and the remaining nerve would be denervated by LDS. From the literature, as described in [46, 49], the renal nerve damage increases the reduction in BP. Furthermore, sympathectomy, which completely destroys sympathetic nerves, also has shown to reduce BP immediately after the procedure and has shown to maintain the reduction [50]. Thus, we expect, the effective nerve damage by LDS combined with laparoscopy would induce an acute decrease in BP and would result in a cascaded BP decrease thereafter.

From the viewpoint of the IDEAL (Idea, Development, Exploration, Assessment, and Long-term monitoring) framework proposed by P. McCulloch et al.[51], our study using LDS is a proof of concept idea and preclinical development for the pathway to technical refinement, stability, and assurance [52]. Through LDS, we expect to provide a solution for controlling lethal resistant hypertension by creating a standardized procedure that is safe and yields possibly similar results between experienced operators and novices. In addition, the system is flexible and adaptable and thus can accommodate renal sympathetic nerves plexus of various sizes. Since the system has the ability to accesses sympathetic nerve directly, it can treat sympathetic nerves located in any proximity of renal artery, e.g., nerves located far from the lumen in the proximal segment of a renal artery, nerves located close to the arterial wall, and nerves inside tunica adventitia of artery [21]. The previous approach, such as the catheter-based RDN, does not have such flexibility and were of limited use. Our LDS approach is innovative, inventive, and opens up the novel opportunity for hypertension treatment. In addition, our proposed system can be expanded to other therapeutic modality as well for treating autonomic nervous system disorders.

VIII. CONCLUSION AND FUTURE WORK

Through mathematical model and simulator study, we established the proof of concept of the novel laparoscopy-based renal denervation system, which employs a direct nerve ablation technique with automated temperature control and flexible electrode to denervate nerves around any artery size. The simulation study using LDS showed that the heat focused on the outer arterial wall while maintaining a constant tip temperature of 65 ℃ for 70 s is a suitable treatment protocol. In the acute swine model study, renal denervation was achieved regardless of nerve size and distribution, resulting in an acute

reduction in blood pressure while preventing arterial damage. Our technology developed and our methodology adopted are sufficient to prove the validity of such an approach, which can be explored further for other applications in addition to hypertension treatment.

This paper focused mainly on demonstrating the feasibility of the proposed novel technology through the mathematic model and in vivo study. We performed laparoscopic renal denervation on the acute swine model and in an open surgery setting to show the effectiveness of the system in vivo. For verifying the efficiency of controlling BP and the safety of the laparoscopic denervation system *in vivo*, further animal studies are needed. As a next step, we plan to conduct animal studies using a survival swine model with the laparoscopic procedure to verify the lowering of BP, neurotransmitter level, and to evaluate whether arterial stenosis by arterial damage is detected after the treatment using the LDS system.

REFERENCES

[1] K. T. Mills *et al.*, "Global disparities of hypertension prevalence and control: a systematic analysis of population-based studies from 90 countries," *Circulation,* vol. 134, no. 6, pp. 441-450, 2016.

[2] H. Salem *et al.*, "WORLDWIDE PREVALENCE OF HYPERTENSION: A POOLED META-ANALYSIS OF 1670 STUDIES IN 71 COUNTRIES WITH 29.5 MILLION PARTICIPANTS," *Journal of the American College of Cardiology,* vol. 71, no. 11 Supplement, p. A1819, 2018.

[3] S. S. Lim *et al.*, "A comparative risk assessment of burden of disease and injury attributable to 67 risk factors and risk factor clusters in 21 regions, 1990–2010: a systematic analysis for the Global Burden of Disease Study 2010," *The lancet,* vol. 380, no. 9859, pp. 2224-2260, 2012.

[4] E. J. Benjamin *et al.*, "Heart disease and stroke statistics-2017 update: a report from the American Heart Association," *Circulation,* vol. 135, no. 10, pp. e146-e603, 2017.

[5] D. A. Calhoun *et al.*, "Resistant hypertension: diagnosis, evaluation, and treatment: a scientific statement from the American Heart Association Professional Education Committee of the Council for High Blood Pressure Research," *Circulation,* vol. 117, no. 25, pp. e510-26, Jun 24 2008.

[6] E. Judd and D. Calhoun, "Apparent and true resistant hypertension: definition, prevalence and outcomes," *Journal of human hypertension,* vol. 28, no. 8, p. 463, 2014.

[7] Y. Sata *et al.*, "Role of the Sympathetic Nervous System and Its Modulation in Renal Hypertension," *Front Med (Lausanne),* vol. 5, p. 82, 2018.

[8] E. V. Allen, "Sympathectomy for essential hypertension," *Circulation,* vol. 6, no. 1, pp. 131-40, Jul 1952.

[9] D. Morrissey *et al.*, "Sympathectomy in the treatment of hypertension review of 122 cases," *The Lancet,* vol. 261, no. 6757, pp. 403-408, 1953.

[10] R. Gulati *et al.*, "The rise, fall, and possible resurrection of renal denervation," *Nat Rev Cardiol,* vol. 13, no. 4, pp. 238-44, Apr 2016.

[11] M. D. Esler *et al.*, "Catheter-based renal denervation for treatment of patients with treatment-resistant hypertension: 36 month results from the SYMPLICITY HTN-2 randomized clinical trial," *Eur Heart J,* vol. 35, no. 26, pp. 1752-9, Jul 2014.

[12] B. Hannawi *et al.*, "Renal Denervation: Past, Present, and Future," *Rev Cardiovasc Med,* vol. 16, no. 2, pp. 114-24, 2015.

[13] H. Krum, *et al.*, "Renal denervation for resistant hypertension—the Symplicity HTN-1 study–Authors' reply," *The Lancet,* vol. 383, no. 9932, pp. 1885-1886, 2014.

[14] D. L. Bhatt *et al.*, "A controlled trial of renal denervation for resistant hypertension," *N Engl J Med,* vol. 370, no. 15, pp. 1393-401, Apr 10 2014.

[15] V. Papademetriou *et al.*, "Renal Denervation and Symplicity HTN-3: "Dubium Sapientiae Initium"(Doubt Is the Beginning of Wisdom)," *Circulation research,* vol. 115, no. 2, pp. 211-214, 2014.

[16] E. E. Vink *et al.*, "Limited destruction of renal nerves after catheter-based renal denervation: results of a human case study," *Nephrol Dial Transplant,* vol. 29, no. 8, pp. 1608-10, Aug 2014.

[17] E. Ye *et al.*, "Design and simulation of novel laparoscopic renal denervation system: a feasibility study," *Int J Hyperthermia,* vol. 35, no. 1, pp. 9-18, 2018.

[18] F. Mahfoud *et al.*, "Comparison of branch and distally focused main renal artery denervation using two different radio-frequency systems in a porcine model," *International journal of cardiology,* vol. 241, pp. 373-378, 2017.

[19] S. Bertog *et al.*, "Randomised, blinded and controlled comparative study of chemical and radiofrequency-based renal denervation in a porcine model," *EuroIntervention: journal of EuroPCR in collaboration with the Working Group on Interventional Cardiology of the European Society of Cardiology,* vol. 12, no. 15, pp. e1898-e1906, 2017.

[20] K. Sakakura *et al.*, "Anatomic assessment of sympathetic peri-arterial renal nerves in man," *J Am Coll Cardiol,* vol. 64, no. 7, pp. 635-43, Aug 19 2014.

[21] W. S. Choe *et al.*, "Anatomic Conformation of Renal Sympathetic Nerve Fibers in Living Human Tissues," *Sci Rep,* vol. 9, no. 1, p. 4831, Mar 18 2019.

[22] A. Diego-Nieto *et al.*, "Severe Renal Artery Stenosis After Renal Sympathetic Denervation," *JACC Cardiovasc Interv,* vol. 8, no. 11, pp. e193-4, Sep 2015.

[23] T. Lambert *et al.*, "Late renal artery stenosis after percutaneous renal denervation," *J Cardiovasc Med (Hagerstown),* vol. 17 Suppl 2, pp. e169-e170, Dec 2016.

[24] A. Cai and D. A. Calhoun, "Resistant Hypertension: An Update of Experimental and Clinical Findings," *Hypertension,* vol. 70, no. 1, pp. 5-9, Jul 2017.

[25] M. R. de Jong *et al.*, "Persistent Increase in Blood Pressure After Renal Nerve Stimulation in Accessory Renal Arteries After Sympathetic Renal Denervation," *Hypertension,* vol. 67, no. 6, pp. 1211-7, Jun 2016.

[26] M. K. Jain and P. D. Wolf, "Temperature-controlled and constant-power radio-frequency ablation: what affects lesion growth?," *IEEE Trans Biomed Eng,* vol. 46, no. 12, pp. 1405-12, Dec 1999.

[27] E. J. Berjano, "Theoretical modeling for radiofrequency ablation: state-of-the-art and challenges for the future," *Biomedical engineering online,* vol. 5, no. 1, p. 24, 2006.

[28] R. K. Chen *et al.*, "Thermoelectrical modeling of bipolar coagulation on posterior spinal artery in a porcine spinal surgery model," *IEEE Transactions on Biomedical Engineering,* vol. 61, no. 1, pp. 182-188, 2014.

[29] J. D. Doss, "Calculation of electric fields in conductive media," *Medical physics,* vol. 9, no. 4, pp. 566-573, 1982.

[30] D. L. Thomas *et al.*, "The measurement of diffusion and perfusion in biological systems using magnetic resonance imaging," *Physics in Medicine and Biology* vol. 45, no. 8, p. R97, 2000.

[31] S. Park *et al.*, "Gelled versus nongelled phantom material for measurement of MRI-induced temperature increases with bioimplants," *IEEE transactions on magnetics,* vol. 39, no. 5, pp. 3367-3371, 2003.

[32] F. A. Duck, "Physical Properties of Tissues: a comprehensive reference book," (in English), *Academic Press,* 2013.

[33] M. Golombeck *et al.*, "Magnetic resonance imaging with implanted neurostimulators: A first numerical approach using finite integration theory," in *International Symposium on Electromagnetic Compatibility: 1999; Magdeburg, Germany*, 1999.

[34] R. H. Edgerton, "Radial conductivity of arterial walls," *Medical and biological engineering,* vol. 13, no. 4, pp. 531-534, 1975.

[35] E. R. Greene *et al.,* "Noninvasive characterization of renal artery blood flow," *Kidney Int,* vol. 20, no. 4, pp. 523-9, Oct 1981.

[36] F. Tian *et al.*, "Absolute measurement of thermal conductivity of poly (acrylic acid) by transient hot wire technique," *Journal of thermal analysis and calorimetry,* vol. 104, no. 3, pp. 823-829, 2011.

[37] S. J. Savader *et al.*, "Volumetric evaluation of blood flow in normal renal arteries with a Doppler flow wire: a feasibility study," *J Vasc Interv Radiol,* vol. 8, no. 2, pp. 209-14, Mar-Apr 1997.

[38] M. W. Dewhirst *et al.*, "Basic principles of thermal dosimetry and thermal thresholds for tissue damage from hyperthermia," *International journal of hyperthermia,* vol. 19, no. 3, pp. 267-294, 2003.

[39] J. A. Pearce, "Comparative analysis of mathematical models of cell death and thermal damage processes," *International Journal of Hyperthermia,* vol. 29, no. 4, pp. 262-280, 2013.

[40] M. Wolf *et al.*, "Procedural and anatomical predictors of renal denervation efficacy using two radiofrequency renal denervation catheters in a porcine model," *Journal of hypertension,* vol. 36, no. 12, p. 2453, 2018.

[41] V. S. Carriel *et al.*, "A novel histochemical method for a simultaneous staining of melanin and collagen fibers," *Journal of Histochemistry & Cytochemistry,* vol. 59, no. 3, pp. 270-277, 2011.

[42] Z. Wang *et al.*, "Comparison of Saline-Irrigated Catheter vs. Temperature-Controlled Catheter for Renal Denervation in a Canine Model," *Am J Hypertens,* vol. 28, no. 12, pp. 1434-43, Dec 2015.

[43] V. Carriel *et al.*, "Differential expression of GAP-43 and neurofilament during peripheral nerve regeneration through bio-artificial conduits," *Journal of tissue engineering and regenerative medicine,* vol. 11, no. 2, pp. 553-563, 2017.

[44] T. Ridler and S. Calvard, "Picture thresholding using an iterative selection method," *IEEE trans syst Man Cybern,* vol. 8, no. 8, pp. 630-632, 1978.

[45] D. C. Gross, "Improving Patient Safety by Quantifying Vascular Tissue Damage from Radio Frequency Induced Heating of Implanted Medical Devices During Magnetic Resonance Imaging," The Ohio State University, 2016.

[46] A. R. Tzafriri *et al.*, "Arterial microanatomy determines the success of energy-based renal denervation in controlling hypertension," *Sci Transl Med,* vol. 7, no. 285, p. 285ra65, Apr 29 2015.

[47] K. Yahagi *et al.*, "ANATOMICAL CONSIDERATIONS FOR RENAL DENERVATION: PERI-ARTERIAL NERVE SIZE DISTRIBUTION IN HEALTHY SWINE," vol. 67, no. 13 Supplement, p. 169, 2016.

[48] A. Tellez *et al.*, "Renal artery nerve distribution and density in the porcine model: biologic implications for the development of radiofrequency ablation therapies," vol. 162, no. 6, pp. 381-389, 2013.

[49] A. R. Tzafriri *et al.*, "Procedural and Anatomical Determinants of Multielectrode Renal Denervation Efficacy," *Hypertension,* vol. 74, no. 3, pp. 546-554, Sep 2019.

[50] V. Papademetriou *et al.*, "Renal Sympathetic Denervation for the Treatment of Difficult-to-Control or Resistant Hypertension," *Int J Hypertens,* vol. 2011, p. 196518, 2011.

[51] P. McCulloch *et al.*, "No surgical innovation without evaluation: the IDEAL recommendations," *The Lancet,* vol. 374, no. 9695, pp. 1105-1112, 2009.

[52] C. Pennell *et al.*, "Practical guide to the Idea, Development and Exploration stages of the IDEAL Framework and Recommendations," *British Journal of Surgery,* vol. 103, no. 5, pp. 607-615, 2016.